BIOCHEMISTRY
including biophysical chemistry & molecular biology
Article

Biochemistry **2009,** *48,* 12145–12158 12145
DOI: 10.1021/bi901672n

Revisiting the Mechanism of Dioxygen Activation in Soluble Methane Monooxygenase from *M. capsulatus* (Bath): Evidence for a Multi-Step, Proton-Dependent Reaction Pathway[†]

Christine E. Tinberg and Stephen J. Lippard*

Department of Chemistry, Massachusetts Institute of Technology, Cambridge, Massachusetts 02139

Received September 24, 2009; Revised Manuscript Received November 16, 2009

ABSTRACT: Stopped-flow kinetic investigations of soluble methane monooxygenase (sMMO) from *M. capsulatus* (Bath) have clarified discrepancies that exist in the literature regarding several aspects of catalysis by this enzyme. The development of thorough kinetic analytical techniques has led to the discovery of two novel oxygenated iron species that accumulate in addition to the well-established intermediates H_{peroxo} and Q. The first intermediate, P*, is a precursor to H_{peroxo} and was identified when the reaction of reduced MMOH and MMOB with O_2 was carried out in the presence of ≥ 540 μM methane to suppress the dominating absorbance signal due to Q. The optical properties of P* are similar to those of H_{peroxo}, with $\varepsilon_{420} = 3500$ M^{-1} cm^{-1} and $\varepsilon_{720} = 1250$ M^{-1} cm^{-1}. These values are suggestive of a peroxo-to-iron(III) charge-transfer transition and resemble those of peroxodiiron(III) intermediates characterized in other carboxylate-bridged diiron proteins and synthetic model complexes. The second identified intermediate, Q*, forms on the pathway of Q decay when reactions are performed in the absence of hydrocarbon substrate. Q* does not react with methane, forms independently of buffer composition, and displays a unique shoulder at 455 nm in its optical spectrum. Studies conducted at different pH values reveal that rate constants corresponding to P* decay/H_{peroxo} formation and H_{peroxo} decay/Q formation are both significantly retarded at high pH and indicate that both events require proton transfer. The processes exhibit normal kinetic solvent isotope effects (KSIEs) of 2.0 and 1.8, respectively, when the reactions are performed in D_2O. Mechanisms are proposed to account for the observations of these novel intermediates and the proton dependencies of P* to H_{peroxo} and H_{peroxo} to Q conversion.

Methane monooxygenases (MMOs[1]) from methanotrophic bacteria catalyze the remarkable oxidation of methane to methanol at ambient temperatures and pressures (*1*). One enzyme responsible for this process in the methanotroph *Methylococcus capsulatus* (Bath), hereafter *Mc*, is soluble methane monooxygenase (sMMO) (*2*). sMMO requires three protein components for efficient catalysis. A dimeric hydroxylase (MMOH) houses two copies of a carboxylate-bridged diiron active site, a reductase (MMOR) acquires electrons from NADH and transfers them to the hydroxylase, and a regulatory protein (MMOB) couples electron consumption to substrate oxidation. The resting state of the hydroxylase (H_{ox}) active site is a di(μ-hydroxo)(μ-carboxylato)diiron(III) species. Upon two-electron reduction to the diiron(II) form (H_{red}), the bridging hydroxide ligands dissociate, and the diiron center reacts rapidly with O_2 in the presence of MMOB. The events that occur as a result of this reaction have been characterized by multiple spectroscopic methods, and a series of oxygenated-iron intermediates accumulate prior to regeneration of the enzyme resting state (*3*−*7*).

Early studies relied on Mössbauer spectroscopy to probe the reaction of $MMOH_{red}$ with O_2 (*6*, *7*). The first species observed by this method after the addition of O_2 is a peroxodiiron(III) unit comprising two antiferromagnetically coupled iron centers of indistinguishable Mössbauer parameters $\delta = 0.66$ mm/s and $\Delta E_Q = 1.51$ mm/s. UV−vis spectroscopy also supported the formation of a peroxodiiron(III) species displaying peroxo-to-iron charge transfer optical bands centered around 720 nm ($\varepsilon = 1800$ M^{-1} cm^{-1}) and 420 nm ($\varepsilon = 4000$ M^{-1} cm^{-1}) as the first observable intermediate (*8*, *9*). The signals arising from Mössbauer and optical spectroscopy were attributed to the same peroxodiiron(III) unit because the decay rates measured by these two methods were identical, and this species was termed H_{peroxo}.[2] The formation rates reported by these two methods differed by an order of magnitude, however. The presence of multiple peroxodiiron(III) species with similar Mössbauer parameters but distinct optical signatures was suggested to explain this disparity, although there was no direct evidence for this proposal. The presence of various peroxodiiron(III) species that

---

[†] This work was funded by grant GM032134 from the National Institute of General Medical Sciences. C.E.T. thanks the NIH for support under Interdepartmental Biotechnology Training Grant T32 GM08334.

*To whom correspondence should be addressed. Tel: (617) 253-1892. Fax: (617) 258-8150. E-mail: lippard@mit.edu.

[1] Abbreviations: MMO, methane monooxygenase; sMMO, soluble methane monooxygenase; MMOH, hydroxylase component of sMMO; MMOB, regulatory component of sMMO; MMOR, reductase protein of sMMO; H_{peroxo}, peroxodiiron intermediate species in MMOH; Q, di(μ-oxo)diiron(IV) intermediate species of MMOH; P*, transient H_{peroxo} precursor; Q*, decay product of Q; MOPS, 3-(*N*-morpholino)propanesulfonic acid; EXAFS, extended X-ray absorption fine structure; KSIE, kinetic solvent isotope effect; RNR, ribonucleotide reductase; T4mo, toluene 4-monooxygenase; T4moD, regulatory component of toluene 4-monooxygenase.

[2] H_{peroxo} is denoted P in studies of sMMO from *M. trichosporium* OB3b.

accumulate on the reaction pathway was later addressed in a study of O_2 activation in MMOH from *M. trichosporium* OB3b, hereafter referred to as *Mt*, which provided direct evidence for an optically distinct H_{peroxo} precursor, P* (*3*). Experiments on the *Mc* enzyme provided no such evidence for this species.

Much effort has been devoted to understanding the nature of H_{peroxo}. Attempts to elucidate the binding mode of the peroxo moiety have been unsuccessful, and there is no consensus on the structure of this intermediate. Analogy to peroxodiiron(III) species generated in other nonheme diiron enzymes, such as those formed in the W48F/D84E variant of ribonucleotide reductase (RNR) (*10*, *11*), at the ferroxidase center of frog M ferritin (*12*), in Δ^9-desaturase (*13*), and in human deoxyhypusine hydroxylase (*14*), supports a symmetric *cis*-μ-1,2 peroxide binding configuration. Some theoretical studies confirm this assignment (*15*), whereas others favor a nonplanar $\mu-\eta^2:\eta^2$ geometry (*16*−*18*). The protonation state of the H_{peroxo} peroxo moiety also remains an unanswered question.

H_{peroxo} oxidizes electron rich substrates such as propylene (*9*) and diethyl ether (*8*); however, in the absence of such substrates it rapidly decays to intermediate Q, an antiferromagnetically coupled diiron(IV) unit responsible for methane oxidation. Structural characterization of Q by EXAFS spectroscopy revealed a short Fe−Fe distance of 2.46 Å from which a di(μ-oxo)diiron(IV) "diamond core" was postulated (*19*). The intense optical bands of Q centered at 350 nm (ε = 3600 M^{-1} cm^{-1}) and 420 nm (ε = 7200 M^{-1} cm^{-1}) that trail into the near-infrared ($\varepsilon_{720} \approx 1000$ M^{-1} cm^{-1}) have been used as a handle for mechanistic studies (*4*−*7*). Q is thought to be responsible for oxidation of a variety of substrates (*3*, *5*, *6*, *9*, *20*), a process that might occur via two single-electron transfer events from substrate to Q in a manner that generates a transient bound radical species (*21*). In the absence of substrate, Q decays slowly to H_{ox} by an unknown pathway that requires the acquisition of two electrons and two protons at the diiron center. The mechanism by which this process occurs has not received much, if any, attention in the literature.

Another enigmatic aspect of MMOH catalysis is the mechanism of H_{peroxo} to Q conversion and concomitant O−O bond cleavage. Two distinct mechanisms have been proposed for this transformation based on existing inorganic chemistry (Scheme 1). The first involves homolytic O−O bond scission and concerted rearrangement of an H_{peroxo} $\mu-\eta^2:\eta^2$ core to form intermediate Q in a manner similar to established peroxodicopper(II) transformations (*22*, *23*). The second includes proton-promoted heterolytic O−O bond cleavage and rearrangement of the diiron center, a mechanism analogous to the generally accepted route of O−O bond scission in cytochrome P450 enzymes (*24*, *25*). Key differences between these two proposed mechanisms are the origin of the two bridging oxygen atoms of Q and the proton requirement for the O−O bond-breaking process.

Scheme 1: Two Possible Mechanisms of O−O Bond Cleavage in MMOH Depicting Oxygen Atoms Derived from O_2 as Filled Circles

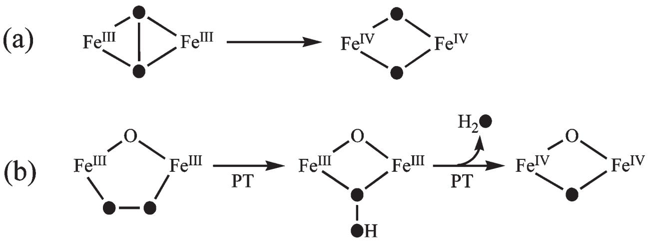

Results from kinetic investigations of the proton requirement of H_{peroxo} to Q conversion in the *Mc* and *Mt* enzymes are contradictory. The rate constants associated with H_{peroxo} formation and H_{peroxo} decay/Q formation in *Mt* MMOH are pH-dependent and display normal solvent kinetic isotope effects (KSIE) in proton inventory studies, results that implicate rate-limiting transfer of a single proton in both steps (*26*). The slopes of the proton inventory plots led the authors to conclude that H_{peroxo} formation and its subsequent conversion to Q involve addition of two protons to an iron-bound peroxide oxygen atom followed by heterolytic O−O bond scission coupled to the release of a water molecule. However, studies of MMO from *Mc* found that these processes were neither pH-dependent nor exhibited KSIEs greater than unity, consistent with proton transfer not being rate-limiting in either of these steps (*6*). A reconciliation of these results is important for understanding the H_{peroxo} to Q pathway and the O−O bond cleavage mechanism in this enzyme, elucidating the protonation state and structure of H_{peroxo}, and guiding experiments to devise synthetic models for the reaction chemistry.

Although these previous studies provide a framework for understanding O_2 activation for attack on the strong and kinetically difficult to access C−H bond of methane, many aspects of MMOH catalysis remain vague. To clarify some of the ambiguities, we have in the present study employed stopped-flow optical spectroscopy to reexamine the mechanism of dioxygen activation in MMOH from *Mc*. Our findings provide direct evidence for a multistep reaction pathway in which a minimum of four oxygenated-iron intermediates accumulate, including P*, previously identified in the *Mt* enzyme, as well as a novel species termed Q*. Q* forms as a result of Q decay and is not reactive toward methane. Comparison of these results to previous work reveals that the H_{peroxo} species formerly characterized by optical and Mössbauer spectroscopy are actually two distinct peroxodiiron(III) intermediates rather than one single entity. Additionally, in contrast with previous reports from the *Mc* enzyme, our data show that H_{peroxo} formation and H_{peroxo} decay/Q formation are both pH-dependent and exhibit normal KIEs, as found for the *Mt* MMOH. The results indicate that both processes involve rate-limiting proton transfer steps, and mechanisms to explain these results are discussed.

MATERIALS AND METHODS

General Considerations. Hydroxylase protein (MMOH) was purified from *Methylococcus capsulatus* (Bath) as previously described, except that a Q Sepharose fast flow anion exchange column (4 × 50 cm) was used in place of the final MonoQ column. Protein obtained by this procedure typically exhibited specific activities of 400−500 mU/mg for propylene oxidation at 45 °C and iron contents of 4.0 ± 0.2 iron atoms per protein dimer (*8*, *9*). The regulatory (MMOB) and reductase (MMOR) proteins were expressed recombinantly in *E. coli* and purified by established methods (*27*, *28*). The buffer system employed in all experiments was 25 mM potassium phosphate ($6.6 \leq pH \leq 8.6$), prepared by adding the appropriate volumes of 1 M K_2HPO_4 and 1 M KH_2PO_4 to ddH_2O and adjusting the pH using HCl or NaOH. Distilled water was deionized with a Milli-Q filtering system. Methane (99.9%) was purchased from Airgas (Independence, OH). All other chemicals were obtained from Aldrich and used as received.

Stopped-Flow Optical Spectroscopy. Single turnover transient kinetic experiments were performed on a Hi-Tech Scientific (Salisbury, UK) SF-61 DX stopped-flow spectrophotomer made anaerobic by flushing the flow circuit extensively with ~10 mM $Na_2S_2O_4$ and then N_2-purged buffer. A protein solution containing $MMOH_{red}$ and 2 equiv of MMOB was prepared by reduction with $Na_2S_2O_4$ in the presence of methyl viologen, as described previously, except that 25 mM potassium phosphate buffer was used instead of MOPS (*9*). Excess reducing agent was removed by dialyzing the mixture twice against 500 mL of buffer for ~1 h each. Following dialysis, the protein was transferred to the anaerobic stopped-flow instrument in a glass tonometer.

For stopped-flow experiments performed in the absence of substrate, reduced protein solution was mixed rapidly with an equal volume of O_2-saturated buffer of the appropriate pH. For experiments performed in the presence of substrate, the reduced protein solution was mixed with an equal volume of buffer containing CH_4 and O_2. Double-mixing stopped-flow (DX-SF) experiments were performed by introducing a solution of substrate-containing buffer at the time of maximization of the intermediate of interest. Substrate solutions were prepared by drawing the appropriate volumes of O_2- and CH_4-saturated buffers into a 10 mL gastight Hamilton syringe. Approximate methane and dioxygen concentrations were calculated using the solubility constants of gaseous CH_4 and O_2 in water at 20 °C, the temperature at which the solutions were prepared (1.54 mM for CH_4 and 1.39 mM for O_2) (*29*).

Q photodecomposes in response to the Xe lamp of the diode array apparatus (*9*); therefore, reactions investigating Q and events resulting from Q decay were all collected at single wavelengths using the photomultiplier tube, limiting the number of data points that could be obtained. Data were collected using Kinetic Studios (Hi-Tech Scientific) and fit with KaleidaGraph v 3.6 (Synergy Software) and Origin v 6.1 (OriginLab Corporation). All experiments were performed at 4 °C. The concentration of MMOH in the optical cell after mixing was 50 μM in all experiments unless otherwise noted. All experiments were carried out at least in triplicate using a minimum of three different batches of proteins.

KSIE Measurements. Deuterium oxide (99.9%) was purchased from Cambridge Isotope Laboratories (Andover, MA). Buffers containing 25 mM potassium phosphate (pD 7.0) were prepared by adding weighed mixtures of K_2HPO_4 and KH_2PO_4 to the appropriate amount of D_2O. The pD of the buffer was adjusted with DCl, where pD = pH meter reading + 0.4. MMOH and MMOB were individually exchanged into D_2O buffer by three repeated rounds of concentration and dilution in Amicon centrifugal concentrators (Millipore, Billerica, MA) over the course of 4 h, which was found to be sufficient for exchange. Protein solutions were prepared and reduced as noted above, except that dialyses were carried out in D_2O buffer for ~1.5 h each. All KSIE experiments were performed at 5 °C. Adequate comparisons to data collected in H_2O at 4 °C could be made because the one degree temperature difference was found to have a negligible effect on the rate constants. Approximate methane concentrations for these experiments were calculated using the solubility constant of gaseous CH_4 in D_2O at 20 °C (1.64 mM) (*29*).

Data Analysis. Except where noted, all experiments were performed under first-order or pseudo first-order conditions and were analyzed accordingly. Multiple chemically reasonable kinetic models were considered when analyzing the results of stopped-flow studies probing the reactions of $MMOH_{red}$ and 2 equiv of MMOB with O_2 and O_2/CH_4 mixtures. The kinetic solutions reported here are those that required the minimum number of variable parameters to adequately fit the data. Data fits were evaluated by examining the magnitude of the difference between the fit and the data at every data point collected (residual plots) and were accepted or rejected on the basis of these fit residuals, the reduced chi-squared value describing the goodness-of-fit ($\chi^2_{red} = \chi^2$/degrees of freedom), and the parameter dependencies.

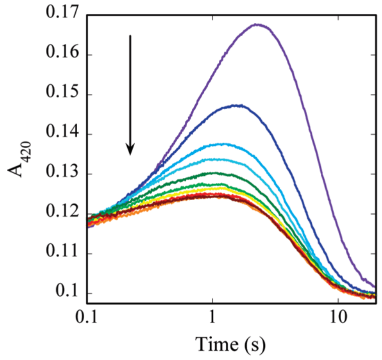

FIGURE 1: Representative 420 nm absorbance profiles for reactions of 50 μM $MMOH_{red}$ and 100 μM MMOB with a mixture of O_2 and CH_4 at pH 7.0 and 4 °C. [CH_4] = 77 μM (purple), 154 μM (blue), 231 μM (cyan), 308 μM (aqua), 385 μM (dark green), 462 μM (light green), 500 μM (yellow), 539 μM (orange), 578 μM (red), and 616 μM (maroon). Data collected on separate occasions with different batches of protein yielded similar results.

RESULTS

$MMOH_{red}$:2B + O_2:Reactions in the Presence of Methane. Results of numerous studies provide compelling evidence that intermediate Q is the oxygenated iron species responsible for methane oxidation, and it is generally accepted that H_{peroxo} does not react with this substrate. To reinvestigate H_{peroxo} formation and decay and to identify other optically significant events that occur prior to formation of Q, we reasoned that the dominant optical signal of Q will be suppressed if sufficiently high concentrations of this substrate are present such that the rate of Q decay exceeds that of its formation. Under these conditions, the weaker optical signatures of preceding intermediates can be uncovered and evaluated by kinetic methods. Stopped-flow optical spectroscopy was therefore employed to monitor the optical changes that occur at 420 nm upon mixing $MMOH_{red}$ and 2 equiv of MMOB with a solution containing O_2 and CH_4 (Figure 1). At low methane concentrations (<~540 μM), the optical signal changes with increasing substrate concentration, suggesting that Q accumulates under these conditions. However, at methane concentrations ≥~540 μM, the optical signal no longer changes with increasing substrate concentration, indicating that Q does not build up, presumably because of rapid reaction with the substrate. Although the optical signal of Q is fully suppressed when [CH_4] ≥ 540 μM, a time-dependent rise and decay in absorbance at 420 nm is observed, indicating the presence of at least one intermediate that is unaffected by methane and absorbs at this wavelength (Figure 1). Because H_{peroxo} absorbs at 420 nm (*8*, *9*), it is reasonable to assume that this intermediate contributes to some of or all of the observed signal.

To investigate the processes associated with the rise and decay in absorbance observed at $[CH_4] \geq 540\ \mu M$ and to determine whether it is solely due to absorbance by H_{peroxo}, data collected under these conditions at 420 and 720 nm were fit using nonlinear least-squares methodology. Previous studies probing the reaction of $MMOH_{red}$ and 2 equiv of MMOB with O_2 have generally relied on fitting single-wavelength data to obtain kinetic information about the processes that occur as a result of this reaction. Here, we found that fitting single-wavelength data sets to sums of exponentials or to analytical kinetic models often resulted in solutions that appeared satisfactory for the data being analyzed but were poor descriptors of data collected under the same conditions at different wavelengths. By fitting data collected at only a single wavelength, it was therefore easy to converge upon an incorrect solution. A more reliable method of fitting the kinetic traces was afforded by collecting data at a minimum of two wavelengths and simultaneously fitting these data sets using shared rate constant parameters (*30*). This approach reduces the number of parameters to be fit by adding constraints and therefore increases our confidence that the model used to fit the data is correct if a satisfactory result is obtained.

Using this method, we observed that the rise and decay in absorbance in the presence of high concentrations of methane did not fit well to a sum of two exponentials describing the process $H_{red} \rightarrow H_{peroxo} \rightarrow H_{ox}$ described previously for *Mc* experiments conducted in the presence of methane (Figure S1a, Supporting Information) (*9*). Instead, the data fit well to a sum of three exponentials representing a minimum of three processes, as reported for the *Mt* system (Figure S1b, Supporting Information) (*3*). Two of those processes must arise from H_{peroxo} formation and from H_{peroxo} decay. The additional feature observed in the data suggests one of the three following possibilities: (i) accumulation of an additional transient species on the reaction pathway, (ii) two productive populations of H_{red} that proceed with different rate constants to H_{peroxo} upon reaction with O_2, or (iii) two pathways that lead to H_{peroxo} decomposition with different rate constants. Although process i seems most likely, processes ii and iii could arise from a heterogeneous population of MMOH/MMOB complexes (*5*) or via a half-sites reactivity mechanism in which the two diiron sites in the hydroxylase react with O_2 on different time scales (*31*). Possibility iii was rejected because truncation of the data to include only points following the time of maximal absorbance fit well to a single exponential decay process. Furthermore, the amplitude describing the additional phase is positive in the exponential fit, suggesting that it contributes to the rise phase of the absorbance profile.

Scheme 2: Models for the Reaction of $MMOH_{red}$ and 2 Equiv of MMOB with O_2 in the Presence of 540 μM Methane

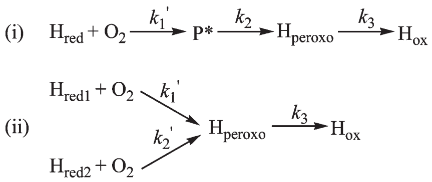

Possibilities i and ii were assessed by fitting the data to differential equations S1 and S2 (Supporting Information) describing the analytical solutions to models i and ii of Scheme 2. H_{peroxo} presumably decays to Q under these conditions; however, because Q is depleted faster than it forms, it does not accumulate and therefore does not have to be accounted for in the kinetic model. Fitting the data to eq S1, which includes an additional intermediate that precedes H_{peroxo} formation, P*, afforded excellent results with $k_1' = 6.7 \pm 0.9\ s^{-1}$, $k_2 = 0.75 \pm 0.04\ s^{-1}$, and $k_3 = 0.34 \pm 0.03\ s^{-1}$ (Figure 2). The values of k_2 and k_3 measured in this work are the same as those reported for H_{peroxo} formation and decay by optical spectroscopy in MOPS buffer (*8*, *9*). We have therefore assigned the second species as H_{peroxo} and the precursor that forms in the faster phase governed by k_1' as the novel transient P*. In contrast, fits to eq S2 (Supporting Information), which yielded similar rate constants, were not as satisfactory (Figure S2, Supporting Information). The best fit from this model resulted when H_{red} comprised 20% of a rapidly reacting diiron population and 80% of a slowly reacting population, which is inconsistent with a half-sites reactivity mechanism. The fits obtained from this model demonstrated unacceptably large parameter error values and a worse χ^2_{red} value than that obtained from fitting to process i. Also, the residual plots from these fits demonstrated sinusoidal behavior indicative of incorrect kinetic modeling. Therefore, both the goodness-of-fit parameters and fit residuals indicate that the $H_{red} \rightarrow P^* \rightarrow H_{peroxo} \rightarrow H_{ox}$ model is more appropriate to describe the data.

*Kinetic Characterization of P**. Data collected at 420 and 720 nm in the presence of 540 μM CH_4 were fit simultaneously to eq S1 (Supporting Information) by sharing rate constant parameters and setting $[H_{red}]_0$ to 32 μM to account for the observation that only 32% of the 100 μM diiron sites in the sample proceed though a productive pathway (*6*). The approximate extinction coefficients obtained were $\varepsilon_{420} \approx 3500\ M^{-1}\ cm^{-1}$ and $\varepsilon_{720} \approx 1250\ M^{-1}\ cm^{-1}$ for P* and $\varepsilon_{420} \approx 3880\ M^{-1}\ cm^{-1}$ and $\varepsilon_{720} \approx 1350\ M^{-1}\ cm^{-1}$ for H_{peroxo}, although these numbers are probably overestimated because the protein preparations used in these studies display significantly higher steady state activities than those previously employed to measure the percentage of active diiron sites (*6*). The similarities between the optical parameters of P* and H_{peroxo} reveal that the two intermediates are electronically identical. The dependence of k_1' on O_2 concentration was measured to probe the mechanism of P* formation. No change was observed for k_1' or for the rate constants governing the subsequent steps when the concentration of O_2 was varied in the experiments and the data were fit to eq S1 (Supporting Information), indicating that the first irreversible step in the reaction precedes P* formation (Figure S3, Supporting Information).

$MMOH_{red}$:2B + O_2: Reactions in the Absence of Methane. Reactions of reduced MMOH and 2 equiv of MMOB with O_2 were monitored to study the events that occur when methane is not present. Previous experiments conducted in MOPS buffer indicated that the data should fit well to an analytical model describing the process $H_{red} \rightarrow H_{peroxo} \rightarrow Q \rightarrow H_{ox}$ (*8*); however, data analyzed simultaneously at 20 different wavelengths spanning from 400 to 740 nm did not fit well to this solution (Figure S4, Supporting Information) or to a sum of three exponentials describing the three processes involved in this model (Figure S5a, Supporting Information). Instead, the data fit well to a sum of four exponentials describing a minimum of four processes (Figure S5b, Supporting Information). The values of the two fastest rate constants obtained from these fits are the same as those of the rate constants describing H_{peroxo} formation (k_2) and decay (k_3) measured in experiments performed in the

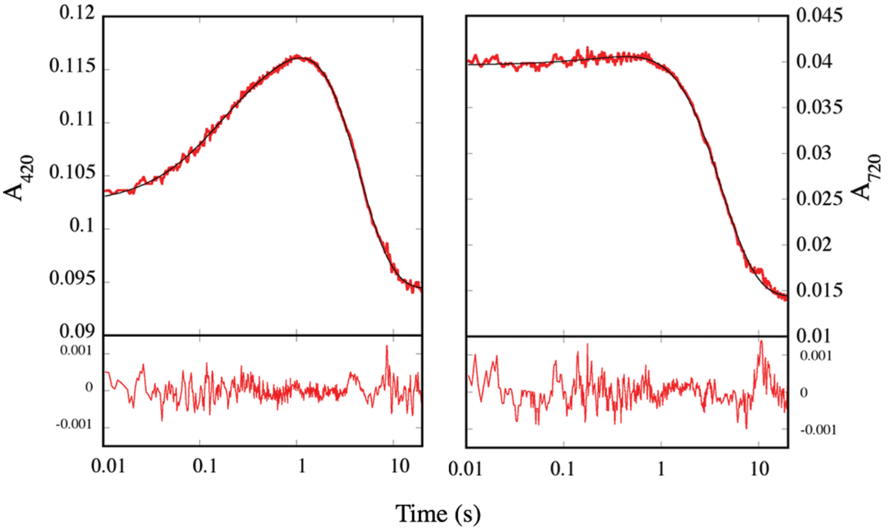

FIGURE 2: Representative fits of data monitoring the reaction of 50 μM $MMOH_{red}$ and 100 μM MMOB with ~210 μM O_2 in the presence of 540 μM CH_4 at pH 7.0 and 4 °C. Data collected at 420 nm (left, red lines) and 720 nm (right, red lines) were fit simultaneously to the $H_{red} \rightarrow P^* \rightarrow H_{peroxo} \rightarrow H_{ox}$ model (eq S1, Supporting Information). This method returned good fits (black lines) with acceptable residuals (bottom plots) and $\chi^2_{red} < 1.07 \times 10^{-7}$.

presence of 540 μM CH_4 (vide supra), allowing us to unambiguously assign these events.[3]

To correlate the two slower observables with enzymatic events, two different chemically reasonable models were considered, and fits of the data to differential equation solutions for these models were compared. The first model describes a process in which a chromophoric intermediate that follows Q decay (denoted Q*) contributes to the observed optical events (iii, Scheme 3). The second model describes a situation in which there are two populations of Q that decay on different time scales (iv, Scheme 3). Fits of the data to eqs S3 and S4 (Supporting Information), the respective differential solutions to models iii and iv, are shown in Figure 3 and Figure S6 (Supporting Information). Fits to model iii afforded excellent results, with $k_2 = 0.75 \pm 0.05$ s^{-1}, $k_3 = 0.37 \pm 0.01$ s^{-1}, $k_4 = 0.011 \pm 0.002$ s^{-1}, and $k_5 = 0.0026 \pm 0.0001$ s^{-1}, whereas those to iv yielded poor fits with sinusoidal residual plots and large parameter dependencies (~1). χ^2_{red} values for fits to iii were over an order of magnitude better than those to iv, allowing us to unambiguously confirm iii as the process with the minimum number of steps necessary to describe the data. Global analysis of kinetic data collected at various wavelengths was employed to approximate the absorption spectrum of Q* (Figure 4). Although spectral determination by this method can be biased by the absorbance of other species present during the reaction, it has been used widely to estimate the optical and fluorescent properties of individual components in complex mixtures (*30*). The optical spectrum of Q* displays a band centered around 420 nm and a shoulder around 455 nm that is not present in the optical spectrum of Q.

Scheme 3: Models for the Reaction of $MMOH_{red}$ and Two Equiv of MMOB with O_2

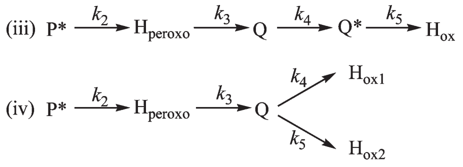

Double-Mixing Stopped Flow Optical Spectroscopy: Q/Q + CH_4.* To address the relative significance of Q and Q* with respect to enzyme function, double mixing stopped-flow experiments were conducted in which either intermediate was generated and then mixed with a solution containing 770 μM CH_4. For each experiment, appropriate age times between the first and second push needed to monitor reactions of Q and Q* were determined by preparing a speciation plot using rate constants extracted from fits of the data to model iii (vide supra) and identifying the t_{max} values of the two intermediates. From this method, t_{max} values of Q and Q* were 13 and 186 s, respectively (Figure 5).

Data investigating reactions of Q with CH_4 at 420 nm were fit well by a single exponential decay process having $k = 3.9 \pm 0.2$ s^{-1} (Figure S7, Supporting Information). This rate constant is ~350 times larger than that for Q decay in the absence of substrate identified in single-mixing experiments (vide supra) and in double-mixing control experiments in which the intermediate was accumulated and mixed with buffer instead of CH_4 ($k_3 = 0.010$ s^{-1}). The acceleration of Q decay in the presence of CH_4 and the fact that a term for Q* is not necessary to fit the data indicate that Q is depleted by a different pathway in the presence of methane than that in its absence. The mechanism of methane-promoted Q decay most likely arises from rapid reaction with this substrate (*3*, *9*).

Experiments probing the reaction of Q* with CH_4 at 420 nm revealed the presence of two distinct decay processes (Figure S7, Supporting Information). Because these two phases are separated by several orders of magnitude in rate constant and are independent of each other (vide infra), the data were fit well by separately

---

[3] The first process $H_{red} \rightarrow P^*$ does not have to be accounted for in these analyses because a significant portion of the rise in absorbance associated with this transformation occurs during the dead time of the stopped-flow instrument and because the process is characterized by only a very modest change in absorbance relative to events that follow. Including an additional term for the first process $H_{red} \rightarrow P^*$ did not reduce the χ^2_{red} of the fit, and the parameter dependency of the rate constant associated with that process was close to unity, suggesting that the inclusion of this step is unnecessary. One assumption implicit in these analyses is that $[P^*] = 0$ at $t = 0$ s. Such is not the case; however, the excellent fits obtained using this model and the fact that the fastest rate constant obtained from these fits matches that of k_2 measured in experiments performed in the presence of 540 μM CH_4 justify this approximation.

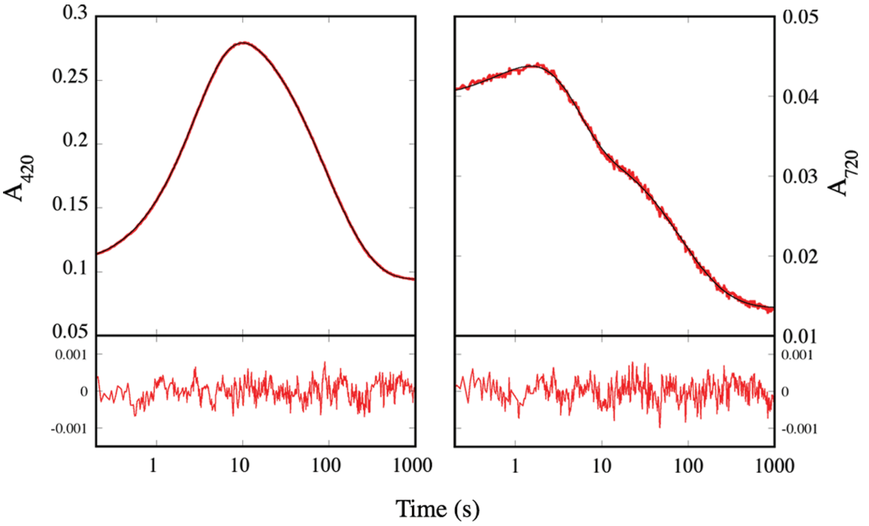

FIGURE 3: Representative fits of data monitoring the reaction of 50 μM $MMOH_{red}$ and 100 μM MMOB with excess O_2 at pH 7.0 and 4 °C. Data collected at 420 nm (left, red lines) and 720 nm (right, red lines) were fit simultaneously to the $P^* \rightarrow H_{peroxo} \rightarrow Q \rightarrow Q^* \rightarrow H_{ox}$ model (eq S3, Supporting Information). This method yielded good fits (black lines) with acceptable residuals (bottom plots) and $\chi^2_{red} < 8.14 \times 10^{-8}$.

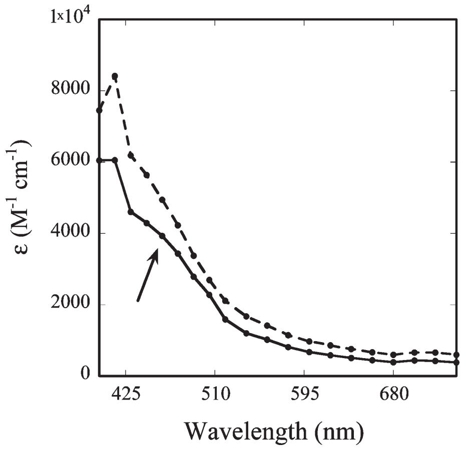

FIGURE 4: Optical spectra of Q (dashed line) and Q* (solid line) recorded at pH 7.0 and converted to molar extinction values. Spectra were obtained at 4 °C from data collected every 15 or 20 nm and analyzed by the global fitting procedures described in the text. The arrow points to the 455 nm shoulder of Q*.

analyzing each event. The rate constants for the two phases obtained by this method are 3.6 ± 0.2 s^{-1} and 0.002 ± 0.001 s^{-1}. The observation that the faster rate constant agrees with that of methane-promoted Q decay (vide supra) allows us to unambiguously assign this process. At the age time employed in these experiments (186 s), the protein sample is a complex mixture of 19% Q, 60% Q*, and 21% H_{ox} (Figure 5), and it is therefore necessary to include a term for the substantial population of Q present because this intermediate absorbs significantly at the wavelength employed (ε_{420} = 8415 M^{-1} cm^{-1}). The rate constant describing the slower event is identical to that of Q* decay measured in single-mixing experiments (vide supra) and in double-mixing control experiments (k_3 = 0.0028 s^{-1}). These results indicate that this process represents Q* decay and that it is not altered by the presence of methane. Although Q is competent for methane oxidation, Q* does not appear to react with this substrate. These conclusions are summarized in Scheme 4.

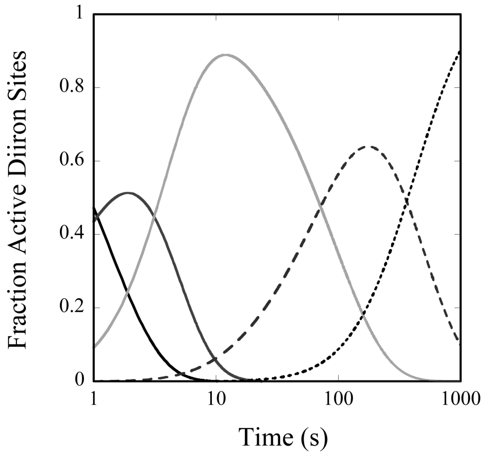

FIGURE 5: Speciation plot depicting the time-dependent formation of transients during the reaction of 50 μM $MMOH_{red}$ and 100 μM MMOB with excess O_2 at pH 7.0 and 4 °C. The concentrations of P* (black solid line), H_{peroxo} (dark gray solid line), Q (light gray solid line), Q* (dark gray large dashed line), and H_{ox} (black small dashed line) as a function of time were calculated from the $P^* \rightarrow H_{peroxo} \rightarrow Q \rightarrow Q^* \rightarrow H_{ox}$ model using rate constants obtained from fits of data to eq S3 (Supporting Information).

Scheme 4: Mechanisms of Q Decay in the Presence of 335 μM CH_4

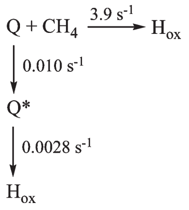

Effect of Buffer on Q Decay. The data strongly suggest that a novel intermediate Q* forms as Q decays in the absence of hydrocarbon substrate. To confirm that Q* is on the reaction pathway and is not a physiologically irrelevant adduct of Q formed by reaction with buffer components, experiments monitoring the reaction of $MMOH_{red}$ and 2 equiv of MMOB with O_2 were performed in 25 mM sodium cacodylate at pH 7.0 (Figure S8, Supporting Information) and in 25 mM MOPS at pH 7.0 (Figure S9, Supporting Information). As for experiments performed in phosphate buffer, data could only be fit well when a fourth term was included in the exponential fit. The data fit nicely

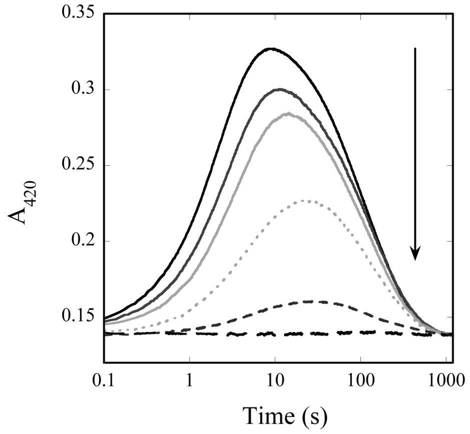

FIGURE 6: Representative 420 nm absorbance profiles monitoring the reactions of 50 μM $MMOH_{red}$ and 100 μM MMOB with excess O_2 at 4°C and pH 6.6 (black solid line), pH 7.2 (dark gray solid line), pH 7.4 (light gray solid line), pH 7.8 (light gray dashed line), pH 8.2 (dark gray dashed line), and pH 8.6 (black dashed line).

to the $P^* \rightarrow H_{peroxo} \rightarrow Q \rightarrow Q^* \rightarrow H_{ox}$ model (eq S3, Supporting Information), and the rate constants obtained from the fits are within error of those measured in phosphate buffer. The exception is k_3, the value of which was reduced to 0.21 s^{-1} in cacodylate buffer. This effect might reflect a steric constraint imposed by large cacodylate molecules on this transformation, which involves geometric reorganization at the diiron center. The necessity of including a term for Q* in all fits indicates that this phenomenon is a property of the protein rather than a result of unnatural buffer−diiron adducts.

These results represent the first evidence for the existence of Q*. Kinetic studies performed previously in MOPS buffer reported that Q decays with a rate constant of 0.05 s^{-1} (*6*, *9*), which is considerably faster than that measured here (0.01 s^{-1}). The fact that Q decay was found to be faster in these earlier studies suggests a reaction of this intermediate with a component not present in the current experiments, which would lead to a mechanism of Q decay that does not proceed through Q*. Results of single- and double-mixing stopped-flow experiments with MOPS reveal that this phenomenon is not due to a difference in buffer composition between these and previous experiments, as we initially suspected (Figures S9 and S10, Supporting Information). The reason for the different Q decay mechanism found in this study therefore remains unknown.

Proton Requirements of $MMOH_{red}$:2B + O_2 Reactions. Reactions of $MMOH_{red}$ and 2 equiv of MMOB with O_2 were monitored in the absence and presence of 540 μM methane at different pH values in the range of 6.6 to 8.6. The enzyme system is stable over the duration of the experiments at all pH values employed. The data clearly demonstrate that buffer pH affects the kinetics of the oxygenated iron intermediates that accumulate (Figure 6). For example, data collected in the absence of methane display time-dependent rise and decay phases at 420 nm when pH < 8.6; however, when the buffer pH is increased, the kinetics of the processes contributing to these features are altered such that the amplitude of the signal is reduced. At pH 8.6, rise and decay processes are no longer observed, indicating that chromophoric intermediates no longer build up under these conditions, either because the kinetics are altered such that they no longer favor accumulation of these species or because the transients do not form under these conditions.

To determine which steps are affected, pH data collected at 420 and 720 nm were fit simultaneously at all pH values employed. Data probing the reactions of $MMOH_{red}$ and 2 equiv of MMOB with O_2 in the presence of methane fit well to eq S1 (Supporting Information) describing Scheme 2i at all pH values employed. Experiments conducted in the absence of methane were analyzed satisfactorily with eq S3 (Supporting Information), the solution to Scheme 3iii.[4] Using these fitting procedures, k_2 and k_3 were found to vary with pH whereas k_1', k_4, and k_5 did not change (Figure 7 and S11, Supporting Information). The values of k_2 and k_3 both decrease with increasing pH, suggesting that the steps associated with these rate constants are facilitated by or dependent on a proton(s). k_2 and k_3 display sigmoidal dependencies on pH, although the experimentally accessible pH range hindered our ability to collect data points near the extrema of each curve where the rate constants flatten out with pH.

The pH titration data for P* to H_{peroxo} conversion (k_2) fit well to eq 1 derived from Scheme 5i, which describes a single, reversible ionization event followed by irreversible conversion of the protonated species to H_{peroxo} (Figure 7a) as follows:

$$k = \frac{k_{HA}10^{(pK_a - pH)}}{1 + 10^{(pK_a - pH)}} + k_A \tag{1}$$

where k_{HA} and k_A are the rate constants of conversion to H_{peroxo} for the protonated and deprotonated species, respectively (*32*). A fit of the data to this model afforded k_{HA} = 1.35 s^{-1}, k_A = 0.08 s^{-1}, and pK_a = 7.2. The small magnitude of k_A and the fact that this number is probably overestimated by our inability to obtain data points at higher pH values strongly suggest that the system does not proceed to H_{peroxo} in the absence of this crucial rate-determining proton transfer step.

The pH titration data for H_{peroxo} to Q conversion (k_3) fit poorly to eq 1 (Figure S12, Supporting Information), with χ^2_{red} = 0.0021, and were much better approximated by eq 2 derived from Scheme 5ii, which describes a doubly ionizing system (Figure 7b) as follows:

$$k = \frac{k_{H_2A}[H^+]^2 + K_1 k_{HA}[H^+] + k_A K_1 K_2}{K_1 K_2 + K_1[H^+] + [H^+]^2} \tag{2}$$

where k_{H2A}, k_{HA}, and k_A are rate constants for conversion of the doubly protonated, singly protonated, and unprotonated species, respectively, K_1 and K_2 are acid dissociation constants for the first and second protonation events, respectively, and $pK_a = -\log(K_a)$ and $pH = -\log([H]^+)$ (*32*). A fit of the data to this model afforded k_{H2A} = 0.41 s^{-1}, k_{HA} = 0.19 s^{-1}, k_A = 0.008 s^{-1}, pK_1 = 7.9, and pK_2 = 7.0. χ^2_{red} for the fit was 0.00028, which is an order of magnitude better than that of the fit to eq 1. These data demonstrate that both the monoprotonated and the diprotonated species are able to generate Q but that the unprotonated form cannot. The rate of conversion of the diprotonated species is approximately twice as fast as that of the monoprotonated species.

---

[4] Data collected in the absence of CH_4 at pH 8.2 fit well to a sum of three exponentials instead of the four describing the $P^* \rightarrow H_{peroxo} \rightarrow Q \rightarrow Q^* \rightarrow H_{ox}$ process required to fit data collected at the other pH values studied. At pH 8.2, the value of k_3 approaches that of k_4 such that Q does not accumulate to a significant amount, and the process does not need to be accounted for. For these fits, the $P^* \rightarrow H_{peroxo} \rightarrow Q \rightarrow Q^* \rightarrow H_{ox}$ model was employed, but k_4 was fixed at 0.0114 s^{-1}, the average value of this pH-independent rate constant across all pH values employed. Acceptable fits were obtained by this method.

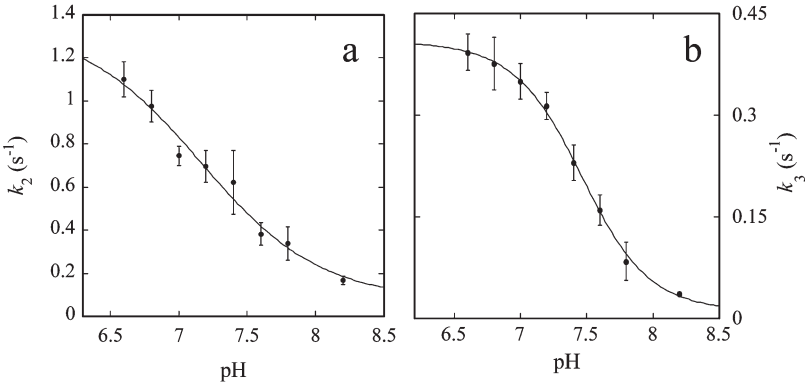

FIGURE 7: pH-dependence of rate contants for (a) P* decay/H_{peroxo} formation, k_2, and (b) H_{peroxo} decay/Q formation, k_3, at 4 °C. Data were collected by mixing 50 μM $MMOH_{red}$ and 100 μM MMOB with excess O_2 and were analyzed as noted in the text. Each data point represents the average of six or more data sets collected in the presence (Scheme 2i) and absence (Scheme 3iii) of 540 μM CH_4 with a minimum of three different batches of protein. P* decay/H_{peroxo} formation data, k_2, (a) fit well to eq 1 describing Scheme 5i, whereas those of H_{peroxo} decay/Q formation data, k_3, (b) were fit to eq 2 describing Scheme 5ii (black lines through points). Error bars depict one standard deviation at the 95% confidence level.

Scheme 5: Models for the pH Dependencies of P* to H_{peroxo} and H_{peroxo} to Q Conversion

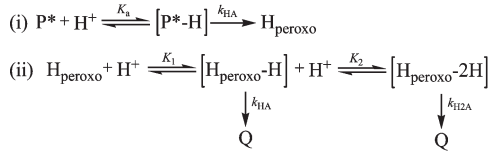

Reactions of $MMOH_{red}$ and 2 equiv of MMOB with O_2 in the absence and presence of CH_4 were also conducted in buffer prepared in D_2O to discern the requirement of solvent-derived protons during the processes monitored. Data fit well in the manner described for reactions of $MMOH_{red}$ and 2 equiv of MMOB with O_2 and O_2/CH_4, delivering $k_1' = 6.5 \pm 2.2$ s^{-1}, $k_2 = 0.38 \pm 0.04$ s^{-1}, $k_3 = 0.20 \pm 0.03$ s^{-1}, $k_4 = 0.013 \pm 0.005$ s^{-1}, and $k_5 = 0.0024 \pm 0.0007$ s^{-1} (Figure S13, Supporting Information). The processes governed by k_2 and k_3 therefore display normal kinetic solvent isotope effects (KSIEs), k_H/k_D, of 2.0 ± 0.2 and 1.8 ± 0.3, respectively, whereas those of k_1', k_4, and k_5 are not affected by isotopic substitution within the error limits of the experiments. The KSIE magnitudes for k_2 and k_3 are typical for proton transfer reactions (*33*).

A concern in devising KSIE experiments is that D_2O is slightly more viscous that H_2O, which can lead to data misinterpretation if not properly accounted for. However, the changes of k_2 and k_3 in response to solvent content monitored here are not likely to arise from the increased viscosity effects. Glycerol affects the single turnover kinetics of this enzyme, but concentrations of this viscogen that mimic the viscosity change of D_2O are insufficient to reproduce the measured KSIE values (*26*, *34*).

Previous kinetic experiments performed in our laboratory suggest that none of the transient events initiated by reaction of $MMOH_{red}$ and 2 equiv of MMOB with O_2 are pH-dependent, nor do they exhibit significant KSIEs (*6*). For the pH-dependence studies, these experiments were performed via pH jump methods in which reduced protein in 10 mM MOPS at pH 7.0 was mixed rapidly with O_2-saturated 100 mM MOPS of the desired pH. However, if reaction with O_2 and subsequent steps are faster than exchange of relevant protons on the protein with bulk solvent, then these effects would not have been detected by using this method. For studies performed in D_2O, the values of the KSIEs are small (≤ 2) and were most likely overlooked.

The data presented here support those reported for the *Mt* enzyme (*26*); however, there are some key differences between the results of the two studies. Both investigations found that the pH dependence of P* to H_{peroxo} conversion fit well to a model consisting of reversible protonation followed by an irreversible step (Scheme 5i). Studies from the *Mt* enzyme showed that the pH dependence of the H_{peroxo} to Q conversion also fit nicely to this model, but the results reported here demonstrate that the model does not adequately represent the data. For the *Mc* enzyme, a model that describes two reversible stepwise protonation events fits the data much better. It seems unlikely that the same intermediate from two closely related sMMO systems requires separate mechanisms for proton transfer; however, the origin of the differences is unknown.

DISCUSSION

The extraordinary ability of methane monooxygenases to catalyze the oxidation of methane selectively to methanol using atmospheric dioxygen has attracted much interest. Whereas experiments probing the mechanism of this transformation have led to the identification of several oxygenated iron intermediate species that are capable of C−H bond abstraction, there are still many questions that remain about events that occur leading up to substrate oxidation and regeneration of the enzyme resting state. In this study, we employed stopped-flow optical spectroscopy to gain insight into the kinetics of the reactions of $MMOH_{red}$ with O_2 in the presence of regulatory protein MMOB.

Origin of Proton Requirement. The demonstration that P* decay/H_{peroxo} formation (k_2) and H_{peroxo} decay/Q formation (k_3) are pH dependent and display normal KSIEs around 2 indicate that proton transfer is involved in the rate-determining steps of these processes. The dependence of these data on preincubation of the protein solution at the pH of interest suggests that an exchangeable proton(s) on the protein in equilibrium with bulk solvent is associated with rate-limiting proton translocation events that give rise to the observed pH and D_2O effects. Although these results verify the necessity of proton transfer for these steps, they cannot definitively describe the location or mechanism of the processes. Translocation of protons could occur at or near the active site or as a result of redox-dependent conformational changes and/or remodeling of protein−protein interactions that alter hydrogen-bonding patterns and accompany structural and electronic changes at the diiron center.

We favor mechanisms for both P* decay/H_{peroxo} formation and H_{peroxo} decay/Q formation in which proton transfer occurs at or near the diiron active site or as a result of very minor structural perturbations instead of large ones. It is likely that large conformational changes or alterations in protein interactions would result in the formation and breakage of many hydrogen bonds rather than involve direct transfer of one or two protons, as the data indicate. Indeed, structural studies on the toluene 4-monooxygenase (T4mo) hydroxylase demonstrated that > 20 new hydrogen bonds form as a result of conformational changes initiated by the binding of its regulatory protein T4moD (*35*). Additionally, the observed KSIEs of ~2.0 are suggestive of direct proton transfer reactions rather than the formation of hydrogen bonds, which usually display small, inverse KSIEs (*36*).

Given these observations, the pH dependencies of k_2 and k_3 are likely to result from proton transfer that occurs at or near the diiron center or from conformational changes restricted to single amino acid side chains that result in proton translocation. Because the MMOH active site cavity is mostly hydrophobic, a large thermodynamic driving force would be necessary to screen the charges that would be generated during the transfer of an active site proton (*15*, *18*, *37*). Therefore, any proton transfer event that occurs at or near the active site should maintain a charge neutral environment and diiron core.

Implications for Proton Transfer Reactions. Inspection of the MMOH active site cavity reveals very few noncoordinated amino acids typically thought to participate in general acid–base catalysis that are located within reasonable proton transfer distance to the iron center (Figure 8). Of those that can potentially participate in such reactions, the only candidates are T213, C151, Q140, D143, and D242. However, none of these amino acids are particularly attractive possibilities because they are all too far from the diiron center to participate in direct proton transfer involving this unit and/or do not display pK_a values near the values measured for k_2 and k_3. Additionally, proton transfer to or from these residues would result in an unlikely active site charge separation. Therefore, this type of mechanism is not anticipated.

A favorable alternative for a proton donor or acceptor is an active site water molecule. Although the pK_a of water is 15.7, this value is significantly reduced by coordination to iron (*38*, *39*). Indeed, terminal Fe(III)–aqua complexes are acidic; for example, the pK_a for deprotonation of $[Fe(H_2O)_6]^{3+}$ is 2.74, and the species exists as $[Fe(OH)(H_2O)_5]^{2+}$ at neutral pH (*40*). Possible candidates for iron-bound proton donors or acceptors with pK_a values in the range of those measured for k_2 and k_3 include terminal aqua or hydroxo groups and/or bridging hydroxide moieties. These possibilities are particularly attractive because proton transfer to/from an iron-bound water-derived molecule from/to another ligand coordinated to the diiron center would maintain a charge-neutral diiron core. Additionally, the proximity of a proton acceptor/donor pair in the case where both units are located at the diiron center is ideal for direct proton transfer. Of special interest to our system is the finding that H^+ addition to a terminal hydroxo group drives the formation of a $[Fe^{IV}_2(\mu\text{-}O)_2]^{4+}$ Q-like species in a synthetic model system (*46*).

Protons could be transferred from a solvent-derived water ligand to a flexible iron ligand. Such an event would maintain a charge-neutral diiron core and might initiate electronic changes at the oxygen–iron unit that promote catalytic events during O_2 activation. Of particular interest is the redox-dependent shifting carboxylate ligand E243, which coordinates in a bidentate fashion, binding to Fe2 and bridging the two iron atoms in the reduced form of the enzyme, but binds in a monodentate manner and only to Fe2 when the iron center is oxidized (*41*, *42*). Departure of E243 from its bridging position may open a coordination site for O_2 to bind and/or accommodate active site structural changes associated with O–O bond cleavage and Q formation. Carboxylate shifts of this kind play an important role in controlling the reactivity of diiron proteins and synthetic model systems (*42*–*44*). It is therefore possible that protonation of E243 provides the driving force that promotes dissociation of this ligand from its bridging position and initiates structural and electronic changes during O_2 activation. Although carboxylate residues are acidic, the hydrophobic nature of the active site might raise the pK_a of E243 to a neutral value. Other amino acid-based possibilities are the coordinating histidines H147 and H246, the protonation of which would most likely also cause these ligands to dissociate. Recent crystallographic studies of the diiron protein *Hedera helix* 18:0 Δ^9-desaturase demonstrated that a histidine ligand undergoes redox-dependent decoordination of exactly this kind (*45*). The pK_a values of histidine residues are within range of those measured for k_2 and k_3.

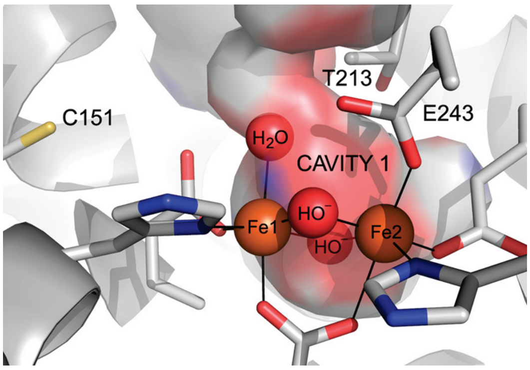

FIGURE 8: $MMOH_{ox}$ active site showing the diiron center, its ligands including the shifting carboxylate E243, and conserved active site hydrophobic residues C151 and T213. The thiol of C151 is located 7.3 Å from Fe1 and the hydroxyl of T213 is positioned 6.8 Å from Fe2. Hydrocarbons are expected to access the diiron site through hydrophobic cavity 1, which is shown as a surface rendering. Relevant atoms or side chains are depicted in ball-and-stick format or as spheres and are colored by atom type (carbon (gray), oxygen (red), nitrogen (blue), sulfur (yellow), iron (orange)). This image was generated in PyMOL (DeLano Scientific LLC) using PBD ID code 1MTY.

One last possibility is that protons are transferred directly to the iron-bound peroxide moiety in these steps. This type of mechanism could result in a hydroperoxo intermediate and facilitate heterolytic O–O bond cleavage, as shown in Scheme 1b. It is invoked in electronically similar cytochrome P450 enzymes (*24*). Protonation of the peroxide could alternatively promote O–O bond cleavage directly. Recent theoretical studies investigating a similar peroxodiiron(III) species in RNR and a mutant form of RNR suggest that H^+ addition to the O–O unit does not result in a stable hydroperoxo species and instead causes O–O bond scission in this enzyme (*47*).

*Identity of P**. Reactions of $MMOH_{red}$ and 2 equiv of MMOB with O_2 performed in the presence of high (≥540 μM) concentrations of CH_4 have provided for the first time in the *Mc* enzyme system direct kinetic evidence for two species that precede Q formation, P* and H_{peroxo}. Comparisons of the data reported here to previous Mössbauer and optical spectroscopic studies are revealing. Mössbauer spectroscopy identified a single peroxodiiron(III) intermediate with $k_{\mathrm{form}} \approx 25\ \mathrm{s}^{-1}$, $k_{\mathrm{decay}} = 0.45\ \mathrm{s}^{-1}$, and $t_{\max} = 156$ ms at 4 °C (*6*). Optical spectroscopic experiments also provided evidence for a single peroxodiiron(III) species, but this unit was characterized by quite different kinetic parameters: $k_{\mathrm{form}} \approx 1.6\ \mathrm{s}^{-1}$, $k_{\mathrm{decay}} = 0.40\ \mathrm{s}^{-1}$, and $t_{\max} = 1-2$ s at 4 °C (*9*). To reconcile the dramatic difference in the formation rate constants observed by these two methods, we proposed the presence of two peroxodiiron(III) species characterized by similar Mössbauer parameters, the first of which was not observable by optical spectroscopy (*9*). Data collected at high concentrations of CH_4 ($\geq$540 μM) presented here unveil the spectrum of P* and provide the first optical evidence for this H_{peroxo} precursor in the *Mc* enzyme. Speciation plots derived from our data lead to the prediction that P* has $t_{\max} = 370$ ms and that H_{peroxo} is characterized by $t_{\max} = 2.1$ s, which is reasonably consistent with the results obtained previously (Figure S14, Supporting Information). However, speciation plots derived from model ii are not consistent with these data, bolstering the argument that this model is not correct (Figure S15, Supporting Information).

Although this work helps to reconcile the differences observed between the two forms of spectroscopy, the rate constant for P* formation measured here is still much lower than that obtained by Mössbauer spectroscopy. Because of the limitations of our instrumentation, the value of k_1' measured here is almost certainly underestimated (and the $t_{\max}$ of P* overestimated) by the fact P* accumulates considerably in the stopped-flow dead time, as evidenced by the fact that the starting absorbances at 420 and 720 nm are much greater than those expected for H_{red} (Figure 2). Therefore, P* might evolve directly from H_{red}, but these data do not rule out the possibility that there is an additional undetected intermediate that forms prior to P*. Similar reasoning led to the proposal of intermediate O, a possible O_2-bound diiron(II) species, in *Mt* MMOH (*3*, *48*).

Because Mössbauer spectroscopy identified only one Q precursor, it is possible that P* and H_{peroxo} exhibit indistinguishable Mössbauer parameters. However, Mössbauer data were not reported in the 0.5−3 s time regime in which H_{peroxo} maximally accumulates according to our optical data (*6*). Without further analysis, we cannot rule out the possibility of distinct parameters for this intermediate. One certainty based on data collected before 0.5 s and the similar $t_{\max}$ values of the species characterized by Mössbauer spectroscopy and P* is that this intermediate is characterized by $\delta = 0.66$ mm/s and $\Delta E_{\mathrm{Q}} = 1.51$ mm/s. Similar Mössbauer parameters have been assigned to a synthetic, structurally characterized (μ-1,2-peroxo)diiron(III) model complex supported by a tris(pyrazolyl)borate ligand scaffold (*49*) as well as the peroxodiiron(III) intermediate generated in the W48A/D84E variant of RNR-R2, both of which feature μ-peroxide binding geometries (*10*, *50*). The absorbance band of P* at 720 nm ($\varepsilon = 1250\ \mathrm{M}^{-1}\ \mathrm{cm}^{-1}$) is similar to those of well-characterized peroxodiiron(III) species in enzymes (*9*, *13*, *51*−*53*) and model systems (*49*, *54*) assigned as peroxo-to-Fe(III) charge transfer transitions. Because of its spectroscopic similarities to those of known enzyme intermediates and model complexes, P* is likely to contain a peroxodiiron(III) unit. Another possibility is a mixed-valent Fe(II)Fe(III) superoxide complex, but this assignment is less likely because the Mössbauer spectrum of such a species should exhibit two distinct quadrupole doublets due to the expected valence localization of the unpaired electrons in this type of system.

The presence of two detectable intermediates that precede Q formation in *Mt* MMOH was previously reported (*3*). The first of these species, P*, forms with a rate constant identical to that of O decay (*26*) and proceeds to intermediate P. The second, P, was reported to absorb minimally at 430 nm, the wavelength at which the data were collected, on the basis of two observations. First, a phase corresponding to P* to P conversion was not necessary to fit data monitored in the absence of substrate, which were modeled well by three phases attributed to O to P*, P to Q, and Q to H_{ox} conversion. Second, the formation of P contributed only a very small amount to the total amplitude of the absorbance rise phase when experiments were performed in the presence of high concentrations of furan to remove optical contributions from Q. The authors argued that the absorbance attributed to this intermediate (H_{peroxo}) at 420 nm in previous reports from our group on the *Mc* system was an artifact from the absorption of Q at this wavelength. However, the data presented here, collected in the presence of methane in which there is no possibility of interference from Q, now provide definitive evidence that H_{peroxo} does indeed absorb strongly at this wavelength and disagree with the results from the *Mt* enzyme.

Nature of P to H_{peroxo} Conversion.* The similarities of the P* optical extinction coefficients to those of H_{peroxo} suggests that these intermediates are electronically and geometrically identical. Analysis of the pH dependent data indicates that a single proton is transferred during the rate-limiting step of P* to H_{peroxo} conversion and that this protonation event, with a pK_{a} of 7.2, must occur for H_{peroxo} to form. As discussed above, this process may involve direct protonation of the O−O moiety or of a coordinating diiron ligand. Formation of a hydroperoxo by protonation of the peroxide, however, would most likely alter the energy of the peroxo-to-iron(III) charge transfer band of P* and the Mössbauer parameters of the species, and the spectroscopic properties of the protonated and unprotonated peroxodiiron(III) species are expected to be different (*55*, *56*). Given this observation, it is most likely that P* to H_{peroxo} conversion occurs via proton transfer to a coordinating amino acid or water-based ligand and not the iron-bound peroxide moiety. For the reasons stated above, we prefer E243 as the proton acceptor. Of relevance to this argument are recent theoretical studies of the peroxo intermediates of RNR and its W48A/Y122F variant (*57*), which find that proton transfer from an iron-bound water molecule or from a solvent-derived proton to a bridging carboxylate ligand are both energetically feasible and result in stable peroxodiiron(III) species (*47*). In the former mechanism, proton transfer occurs with concomitant opening of the bidentate carboxylate bridge. These findings, the necessity of E243 to dissociate from its bridging position to accommodate structural changes associated with H_{peroxo} to Q conversion, and the potential of a hydrophobic active site to raise the pK_{a} of this carboxylate suggest the mechanism presented in Scheme 6.

Nature of H_{peroxo} to Q Conversion. The ability of sMMO to provide a single oxygen atom from molecular oxygen for incorporation into hydrocarbon substrates depends on its ability to cleave the O−O bond and form a potent oxidant. O−O bond scission occurs concomitant with H_{peroxo} to Q conversion; however, the mechanistic details of this step are not well understood. Scheme 1 depicts two simplified mechanisms for this event in which O−O bond cleavage processes are either homolytic (Scheme 1a) or heterolytic (Scheme 1b). In principle, the products of steady state reaction of the enzyme with substrate using $^{18}O_2$ might discriminate between these mechanisms. Product is

Scheme 6: One Possible Mechanism of P* to H_{peroxo} Conversion Depicting Only Key Iron Ligands

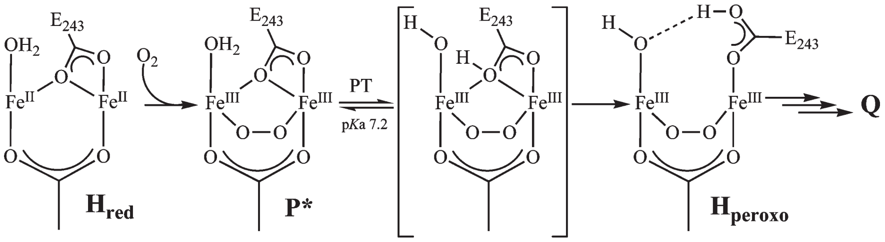

Scheme 7: One Possible Mechanism of H_{peroxo} to Q Conversion Depicting Only Key Iron Ligands and the Oxygen Atoms Derived from O_2 as Filled Circles

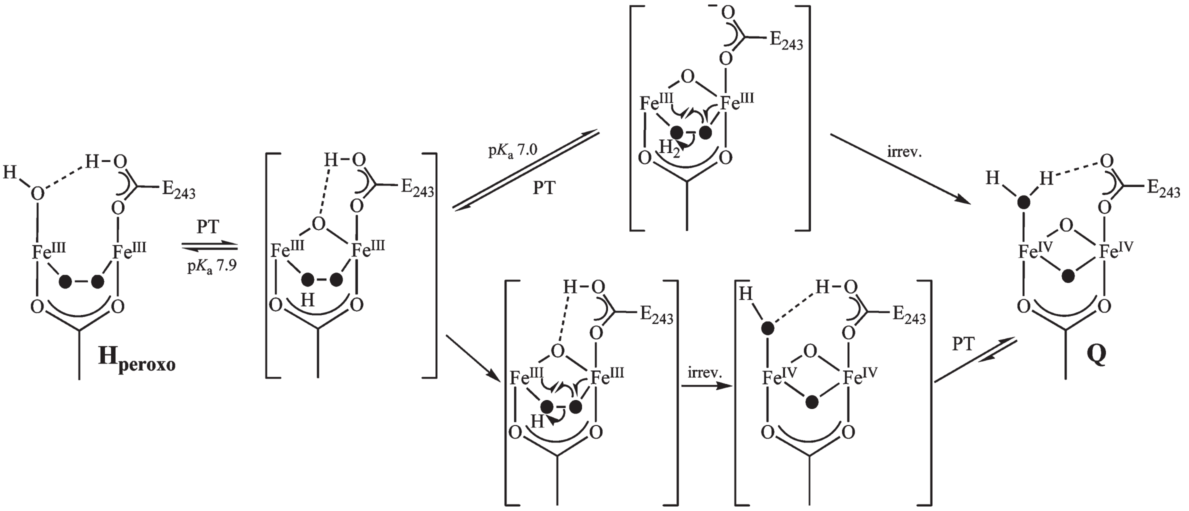

expected to be completely labeled if both oxygen atoms of Q derive from O_2, but might contain a mixture of ^{16}O and ^{18}O labels if a solvent-derived oxygen atom were incorporated into Q. Such a study did reveal that 100% of label is incorporated into methanol (*58*), in support of a homolytic mechanism. However, this interpretation is not definitive because the second labeled oxygen atom might be retained in the active site. In this manner, 100% of the label could be incorporated into the product, even when the O−O bond is cleaved heterolytically.

Analysis of the pH dependence data suggests that two protons can be transferred before the first irreversible step of H_{peroxo} to Q conversion. Whereas one protonation event, with a pK_a of 7.9, is crucial for Q formation, the second, with a pK_a of 7.0, accelerates the rate of conversion of the monoprotonated species but is not required. The absolute necessity of the first protonation step suggests that it occurs directly at the iron center and facilitates O−O bond cleavage. One possible mechanism of H_{peroxo} to Q conversion is depicted in Scheme 7. In this mechanism, a first and necessary proton transfer occurs from a terminal hydroxide, forming a hydroperoxide and an oxo bridge. The O−O bond of the hydroperoxide can then be cleaved heterolytically to form a transient Fe_2^{IV} species with a terminal hydroxide. Proton transfer from E243 after irreversible O−O bond cleavage could then generate Q. Whereas this single proton transfer pathway is sufficient for Q formation, a second protonation at the peroxide moiety, characterized by a pK_a of 7.0, might lead to more rapid O−O bond scission. The O−O bond breakage process is depicted to occur via a concerted heterolytic mechanism but might involve the generation of a transient $Fe^{III}Fe^{V}$ terminal oxo species (*59*).

Mechanism of Q Decay. The mechanism of Q decay in the absence of substrates has remained an enigma for many years. This reaction requires the acquisition of two protons and two electrons at the diiron active site, but the source of these substrates is unknown. Protons could derive from solvent; however, because there are no exogenous electron donors in the reaction mixture, the electrons must come from the protein itself. Two possible protein-based reductants can be envisioned in this system: amino acid side chains and/or a diiron(II) center in the neighboring MMOH protomer (Scheme 8). For the former, Q could abstract electrons and possibly protons from a nearby amino acid residue. This process could be achieved either by direct oxidative hydroxylation of a proximal amino acid residue (Scheme 8a) or by two stepwise electron transfer events, most likely proton-coupled (Scheme 8b). The latter option would generate a protein-based radical and a mixed valent $Fe^{III}Fe^{IV}$ center and is reminiscent of chemistry occurring in the R2 subunit of RNR, in which the nearby amino acids W48 and Y122 can donate electrons to the iron site during formation of the $Fe^{III}Fe^{IV}$ intermediate X (Scheme 8c) (*60*, *61*). For the second option, it is possible that electrons from a neighboring diiron(II) center could quench Q, as proposed to explain the formation of $Fe^{III}Fe^{IV}$ and $Fe^{II}Fe^{III}$ species in the reaction of a synthetic tetracarboxylate diiron(II) model system with O_2 (*62*). If a diiron(II) center were present in the active site of one hydroxylase protomer when Q had formed in the other, intramolecular electron transfer between the diiron centers could lead to the formation of two diiron(III) H_{ox} species. Indeed, a large population of H_{red} decays to H_{ox} by an unknown mechanism on a time scale that is much slower than the O_2 activation phase (*6*), and therefore, a significant portion diiron(II) is available to donate electrons to Q. However, this

Scheme 8: Possible Mechanisms of Q Decay in the Absence of Hydrocarbon Substrates

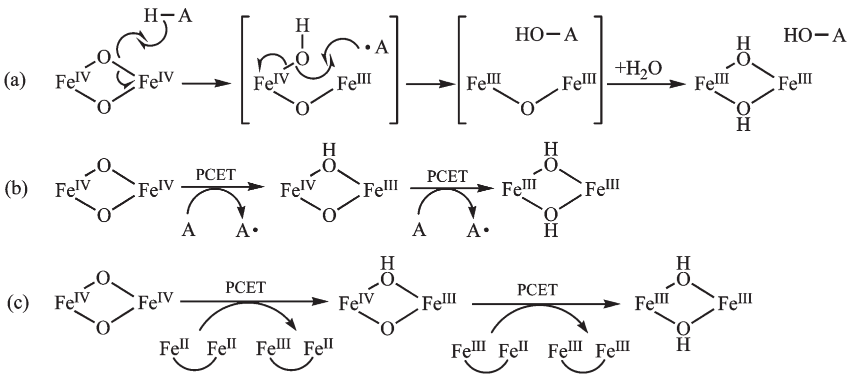

possibility seems less likely considering that the distance between the two iron centers is ~45 Å (*63*), an unprecedented distance for protein electron transfer.

The data reported here suggest for the first time an intermediate species, Q*, which forms as a result of Q decay in the absence of hydrocarbon substrates. Two lines of evidence indicate that Q* is an intermediate on the Q decay pathway rather than a functionally significant species. First, Q* is not capable of methane oxidation, and second, Q reacts with methane and does so by a mechanism that does not proceed through Q*. This intermediate could be composed of an $Fe^{III}Fe^{IV}$ unit and a protein-based radical (Scheme 8b) or a combination of $Fe^{III}Fe^{IV}$ and $Fe^{II}Fe^{III}$ species (Scheme 8c), both of which are consistent with its optical spectrum. It is also possible that Q* is a rearranged thermodynamically stable Fe^{IV}_2 product of Q. Spectroscopic characterization of intermediate Q* is currently in progress to investigate the nature of this species.

CONCLUDING REMARKS

The data presented here provide conclusive kinetic evidence for the presence of multiple oxygenated diiron intermediates that accumulate during MMOH O_2 activation and demonstrate that P* to H_{peroxo} and H_{peroxo} to Q conversion are both pH dependent. These studies and recent investigations of other BMMs and model complexes highlight the complexity of the systems, particularly with respect to the coordination of O_2 activation with proton translocation, electron transfer, and hydrocarbon entry and egress. Taken together, the present study and prior work on the *Mt* system have now begun to converge, providing a framework for understanding MMOH catalysis and a paradigm for interpreting kinetic data in this system. However, questions raised by these studies indicate the need for further kinetic and spectroscopic evaluation. For example, the nature of the proton transfer events during P* to H_{peroxo} and H_{peroxo} to Q conversion and the electronic and geometric identities of the four intermediates are pressing, unsolved questions. Efforts are therefore under way to reinvestigate the spectroscopic properties and protonation states of P*, H_{peroxo}, and Q, and to determine those of Q*.

ACKNOWLEDGMENT

We thank Dr. R. K. Behan and Ms. W. J. Song for helpful discussions.

SUPPORTING INFORMATION AVAILABLE

Equations S1−S4, derivations of eqs S2, S3, and S4, Table S1 containing rate constants for the O_2 activation processes at all pH values employed, Figures S1−S15. This material is available free of charge via the Internet at http://pubs.acs.org.

REFERENCES

1. Merkx, M., Kopp, D. A., Sazinsky, M. H., Blazyk, J. L., Müller, J., and Lippard, S. J. (2001) Dioxygen Activation and Methane Hydroxylation by Soluble Methane Monooxygenase: A Tale of Two Irons and Three Proteins. *Angew. Chem., Int. Ed. 40*, 2782–2807.
2. Hakemian, A. S., and Rosenzweig, A. C. (2007) The Biochemistry of Methane Oxidation. *Annu. Rev. Biochem. 76*, 223–241.
3. Brazeau, B. J., and Lipscomb, J. D. (2000) Kinetics and Activation Thermodynamics of Methane Monooxygenase Compound Q Formation and Reaction with Substrates. *Biochemistry 39*, 13503–13515.
4. Lee, S.-K., Fox, B. G., Froland, W. A., Lipscomb, J. D., and Münck, E. (1993) A Transient Intermediate of the Methane Monooxygenase Catalytic Cycle Containing an $Fe^{IV}Fe^{IV}$ Cluster. *J. Am. Chem. Soc. 115*, 6450–6451.
5. Lee, S.-K., Nesheim, J. C., and Lipscomb, J. D. (1993) Transient Intermediates of the Methane Monooxygenase Catalytic Cycle. *J. Biol. Chem. 268*, 21569–21577.
6. Liu, K. E., Valentine, A. M., Wang, D., Huynh, B. H., Edmondson, D. E., Salifoglou, A., and Lippard, S. J. (1995) Kinetic and Spectroscopic Characterization of Intermediates and Component Interactions in Reactions of Methane Monooxygenase from *Methylococcus capsulatus* (Bath). *J. Am. Chem. Soc. 117*, 10174–10185.
7. Liu, K. E., Wang, D., Huynh, B. H., Edmondson, D. E., Salifoglou, A., and Lippard, S. J. (1994) Spectroscopic Detection of Intermediates in the Reaction of Dioxygen with Reduced Methane Monooxygenase Hydroxylase from *Methylococcus capsulatus* (Bath). *J. Am. Chem. Soc. 116*, 7465–7466.
8. Beauvais, L. G., and Lippard, S. J. (2005) Reactions of the Peroxo Intermediate of Soluble Methane Monooxygenase Hydroxylase with Ethers. *J. Am. Chem. Soc. 127*, 7370–7378.
9. Valentine, A. M., Stahl, S. S., and Lippard, S. J. (1999) Mechanistic Studies of the Reaction of Reduced Methane Monooxygenase Hydroxylase with Dioxygen and Substrates. *J. Am. Chem. Soc. 121*, 3876–3887.
10. Moënne-Loccoz, P., Baldwin, J., Ley, B. A., Loehr, T. M., and Bollinger, J. M., Jr. (1998) O_2 Activation by Non-Heme Diiron Proteins: Identification of a Symmetric μ-1,2-Peroxide in a Mutant of Ribonucleotide Reductase. *Biochemistry 37*, 14659–14663.
11. Skulan, A. J., Brunold, T. C., Baldwin, J., Saleh, L., Bollinger, J. M., Jr., and Solomon, E. I. (2004) Nature of the Peroxo Intermediate of the W48F/D84E Ribonucleotide Reductase Variant: Implications for O_2 Activation by Binuclear Non-Heme Iron Enzymes. *J. Am. Chem. Soc. 126*, 8842–8855.
12. Moënne-Loccoz, P., Krebs, C., Herlihy, K., Edmondson, D. E., Theil, E. C., Huynh, B. H., and Loehr, T. M. (1999) The Ferroxidase Reaction of Ferritin Reveals a Diferric μ-1,2 Bridging Peroxide Intermediate in Common with Other O_2-Activating Non-Heme Diiron Proteins. *Biochemistry 38*, 5290–5295.
13. Broadwater, J. A., Ai, J., Loehr, T. M., Sanders-Loehr, J., and Fox, B. G. (1998) Peroxodiferric Intermediate of Stearoyl-Acyl Carrier Protein Δ^9 Desaturase: Oxidase Reactivity during Single Turnover and Implications for the Mechanism of Desaturation. *Biochemistry 37*, 14664–14671.
14. Vu, V. V., Emerson, J. P., Martinho, M., Kim, Y. S., Münck, E., Park, M. H., and Que, L., Jr. (2009) Human Deoxyhypusine Hydroxylase, an Enzyme Involved in Regulating Cell Growth, Activates O_2 with a

Nonheme Diiron Center. *Proc. Natl. Acad. Sci. U.S.A. 106*, 14814–14819.

15. Han, W.-G., and Noodleman, L. (2008) Structural Model Studies for the Peroxo Intermediate P and the Reaction Pathway from P → Q of Methane Monooxygenase Using Broken-Symmetry Density Functional Calculations. *Inorg. Chem. 47*, 2975–2986.
16. Gherman, B. F., Baik, M.-H., Lippard, S. J., and Friesner, R. A. (2004) Dioxygen Activation in Methane Monooxygenase: A Theoretical Study. *J. Am. Chem. Soc. 126*, 2978–2990.
17. Rinaldo, D., Philipp, D. M., Lippard, S. J., and Friesner, R. A. (2007) Intermediates in Dioxygen Activation by Methane Monooxygenase: A QM/MM Study. *J. Am. Chem. Soc. 129*, 3135–3147.
18. Siegbahn, P. E. M. (2001) O−O Bond Cleavage and Alkane Hydroxylation in Methane Monooxygenase. *J. Biol. Inorg. Chem. 6*, 27–45.
19. Shu, L., Nesheim, J. C., Kauffmann, K., Münck, E., Lipscomb, J. D., and Que, L., Jr. (1997) An $Fe_2^{IV}O_2$ Diamond Core Structure for the Key Intermediate Q of Methane Monooxygenase. *Science 275*, 515–518.
20. Ambundo, E. A., Friesner, R. A., and Lippard, S. J. (2002) Reactions of Methane Monooxygenase Intermediate Q with Derivatized Methanes. *J. Am. Chem. Soc. 124*, 8770–8771.
21. Baik, M.-H., Gherman, B. F., Friesner, R. A., and Lippard, S. J. (2002) Hydroxylation of Methane by Non-Heme Diiron Enzymes: Molecular Orbital Analysis of C-H Bond Activation by Reactive Intermediate Q. *J. Am. Chem. Soc. 124*, 14608–14615.
22. Halfen, J. A., Mahapatra, S., Wilkinson, E. C., Kaderli, S., Young, V. G., Jr., Que, L., Jr., Zuberbühler, A. D., and Tolman, W. B. (1996) Reversible Cleavage and Formation of the Dioxygen O−O Bond Within a Dicopper Complex. *Science 271*, 1397–1400.
23. Lewis, E. A., and Tolman, W. B. (2004) Reactivity of Dioxygen-Copper Systems. *Chem. Rev. 104*, 1047–1076.
24. Denisov, I. G., Makris, T. M., Sligar, S. G., and Schlichting, I. (2005) Structure and Chemistry of Cytochrome P450. *Chem. Rev. 105*, 2253–2277.
25. Nam, W. (2007) High-Valent Iron(IV)-Oxo Complexes of Heme and Non-Heme Ligands in Oxygenation Reactions. *Acc. Chem. Res. 40*, 522–531.
26. Lee, S.-K., and Lipscomb, J. D. (1999) Oxygen Activation Catalyzed by Methane Monooxygenase Hydroxylase Component: Proton Delivery during the O−O Bond Cleavage Steps. *Biochemistry 38*, 4423–4432.
27. Coufal, D. E., Blazyk, J. L., Whittington, D. A., Wu, W. W., Rosenzweig, A. C., and Lippard, S. J. (2000) Sequencing and Analysis of the *Methylococcus capsulatus* (Bath) Soluble Methane Monooxygenase Genes. *Eur. J. Biochem. 267*, 2174–2185.
28. Kopp, D. A., Gassner, G. T., Blazyk, J. L., and Lippard, S. J. (2001) Electron-Transfer Reactions of the Reductase Component of Soluble Methane Monooxygenase from *Methylococcus capsulatus* (Bath). *Biochemistry 40*, 14932–14941.
29. Wilhelm, E., Battino, R., and Wilcock, R. J. (1977) Low-Pressure Solubility of Gases in Liquid Water. *Chem. Rev. 77*, 219–262.
30. Beechem, J. M. (1992) Global Analysis of Biochemical and Biophysical Data. *Methods Enzymol. 210*, 37–54.
31. Murray, L. J., and Lippard, S. J. (2007) Substrate Trafficking and Dioxygen Activation in Bacterial Multicomponent Monooxygenases. *Acc. Chem. Res. 40*, 466–474.
32. Fersht, A. (1977) Enzyme Structure and Mechanism , 2nd ed., Chapter 5, W. H. Freeman and Co., New York, NY.
33. Quinn, D. M., and Sutton, L. D. (1991) Theoretical Basis and Mechanistic Utility of Solvent Isotope Effects, in Enzyme Mechanism from Isotope Effects (Cook, P. F., Ed.) CRC Press, Boca Raton, FL.
34. Tinberg, C. E., and Lippard, S. J. (2009) Unpublished results.
35. Bailey, L. J., McCoy, J. G., Phillips, G. N., Jr., and Fox, B. G. (2008) Structural Consequences of Effector Protein Complex Formation in a Diiron Hydroxylase. *Proc. Natl. Acad. Sci. U.S.A. 105*, 19194–19198.
36. Schowen, K. B., and Schowen, R. L. (1982) Solvent Isotope Effects on Enzyme Systems. *Methods Enzymol. 87*, 551–606.
37. Dunietz, B. D., Beachy, M. D., Cao, Y., Whittington, D. A., Lippard, S. J., and Friesner, R. A. (2000) Large Scale ab Initio Quantum Chemical Calculation of the Intermediates in the Soluble Methane Monooxygenase Catalytic Cycle. *J. Am. Chem. Soc. 122*, 2828–2839.
38. Holm, R. H., Kennepohl, P., and Solomon, E. I. (1996) Structural and Functional Aspects of Metal Sites in Biology. *Chem. Rev. 96*, 2239–2314.
39. Lippard, S. J., and Berg, J. M. (1994) Priciples of Bioinorganic Chemistry, pp 24−26, University Science Books, Mill Valley, CA.
40. Cotton, F. A., Wilkinson, G., Murillo, C. A., and Bochmann, M. (2003) Advanced Inorganic Chemistry , 6th ed., p 787, John Wiley & Sons, Inc, New York.
41. Whittington, D. A., and Lippard, S. J. (2001) Crystal Structures of the Soluble Methane Monooxygenase Hydroxylase from *Methylococcus capsulatus* (Bath) Demonstrating Geometrical Variability at the Dinuclear Iron Active Site. *J. Am. Chem. Soc. 123*, 827–838.
42. Sazinsky, M. H., and Lippard, S. J. (2006) Correlating Structure with Function in Bacterial Multicomponent Monooxygenases and Related Diiron Proteins. *Acc. Chem. Res. 39*, 558–566.
43. Rardin, R. L., Tolman, W. B., and Lippard, S. J. (1991) Monodentate Carboxylate Complexes and the Carboxylate Shift - Implications for Polymetalloprotein Structure and Function. *New J. Chem. 15*, 417–430.
44. Tshuva, E. Y., and Lippard, S. J. (2004) Synthetic Models for Non-Heme Carboxylate-Bridged Diiron Metalloproteins: Strategies and Tactics. *Chem. Rev. 104*, 987–1012.
45. Shanklin, J., Guy, J. E., Mishra, G., and Lindqvist, Y. (2009) Desaturases: Emerging Models for Understanding Functional Diversification of Diiron-Containing Enzymes. *J. Biol. Chem. 284*, 18559–18563.
46. Xue, G., Fiedler, A. T., Martinho, M., Münck, E., and Que, L., Jr. (2008) Insights into the P-to-Q Conversion in the Catalytic Cycle of Methane Monooxygenase from a Synthetic Model System. *Proc. Natl. Acad. Sci. U.S.A. 105*, 20615–20620.
47. Jensen, K. P., Bell, C. B., III, Clay, M. D., and Solomon, E. I. (2009) Peroxo-Type Intermediates in Class I Ribonucleotide Reductase and Related Binuclear Non-Heme Iron Enzymes. *J. Am. Chem. Soc. 131*, 12155–12171.
48. Liu, Y., Nesheim, J. C., Lee, S.-K., and Lipscomb, J. D. (1995) Gating Effects of Component B on Oxygen Activation by the Methane Monooxygenase Hydroxylase Component. *J. Biol. Chem. 270*, 24662–24665.
49. Kim, K., and Lippard, S. J. (1996) Structure and Mössbauer Spectrum of a (μ-1,2-Peroxo)bis(μ-carboxylato)diiron(III) Model for the Peroxo Intermediate in the Methane Monooxygenase Hydroxylase Reaction Cycle. *J. Am. Chem. Soc. 118*, 4914–4915.
50. Baldwin, J., Krebs, C., Saleh, L., Stelling, M., Huynh, B. H., Bollinger, J. M., Jr., and Riggs-Gelasco, P. (2003) Structural Characterization of the Peroxodiiron(III) Intermediate Generated during Oxygen Activation by the W48A/D84E Variant of Ribonucleotide Reductase Protein R2 from *Escherichia coli*. *Biochemistry 42*, 13269–13279.
51. Bollinger, J. M., Jr., Krebs, C., Vicol, A., Chen, S., Ley, B. A., Edmondson, D. E., and Huynh, B. H. (1998) Engineering the Diiron Site of *Escherichia coli* Ribonucleotide Reductase Protein R2 to Accumulate an Intermediate Similar to H_{peroxo}, the Putative Peroxodiiron(III) Complex from the Methane Monooxygenase Catalytic Cycle. *J. Am. Chem. Soc. 120*, 1094–1095.
52. Pereira, A. S., Small, W., Krebs, C., Tavares, P., Edmondson, D. E., Theil, E. C., and Huynh, B. H. (1998) Direct Spectroscopic and Kinetic Evidence for the Involvement of a Peroxodiferric Intermediate during the Ferroxidase Reaction in Fast Ferritin Mineralization. *Biochemistry 37*, 9871–9876.
53. Song, W. J., Behan, R. K., Naik, S. G., Huynh, B. H., and Lippard, S. J. (2009) Characterization of a Peroxodiiron(III) Intermediate in the T201S Variant of Toluene/*o*-Xylene Monooxygenase Hydroxylase from *Pseudomonas sp.* OX1. *J. Am. Chem. Soc. 131*, 6074–6075.
54. Yamashita, M., Furutachi, H., Tosha, T., Fujinami, S., Saito, W., Maeda, Y., Takahashi, K., Tanaka, K., Kitagawa, T., and Suzuki, M. (2007) Regioselective Arene Hydroxylation Mediated by a (μ-Peroxo)diiron(III) Complex: A Functional Model for Toluene Monooxygenase. *J. Am. Chem. Soc. 129*, 2–3.
55. Liu, J.-G., Ohta, T., Yamaguchi, S., Ogura, T., Sakamoto, S., Maeda, Y., and Naruta, Y. (2009) Spectroscopic Characterization of a Hydroperoxo-Heme Intermediate: Conversion of a Side-On Peroxo to an End-On Hydroperoxo Complex. *Angew. Chem. Int. Ed. 48*, 1–6.
56. Roelfes, G., Vrajmasu, V., Chen, K., Ho, R. Y. N., Rohde, J.-U., Zondervan, C., la Crois, R. M., Schudde, E. P., Lutz, M., Spek, A. L., Hage, R., Feringa, B. L., Münck, E., and Que, L., Jr. (2003) End-On and Side-On Peroxo Derivatives of Non-Heme Iron Complexes with Pentadentate Ligands: Models for Putative Intermediates in Biological Iron/Dioxygen Chemistry. *Inorg. Chem. 42*, 2639–2653.
57. Saleh, L., Krebs, C., Ley, B. A., Naik, S., Huynh, B. H., and Bollinger, J. M., Jr. (2004) Use of a Chemical Trigger for Electron Transfer to Characterize a Precursor to Cluster X in Assembly of the Iron-Radical Cofactor of *Escherichia coli* Ribonucleotide Reductase. *Biochemistry 43*, 5953–5964.
58. Nesheim, J. C., and Lipscomb, J. D. (1996) Large Kinetic Isotope Effects in Methane Oxidation Catalyzed by Methane

Monooxygenase: Evidence for C-H Bond Cleavage in a Reaction Cycle Intermediate. *Biochemistry 35*, 10240–10247.

59. Rowe, G. T., Rybak-Akimova, E. V., and Caradonna, J. P. (2007) Unraveling the Reactive Species of a Functional Non-Heme Iron Monooxygenase Model Using Stopped-Flow UV-Vis Spectroscopy. *Inorg. Chem. 46*, 10594–10606.
60. Krebs, C., Chen, S., Baldwin, J., Ley, B. A., Patel, U., Edmondson, D. E., Huynh, B. H., and Bollinger, J. M., Jr. (2000) Mechanism of Rapid Electron Transfer during Oxygen Activation in the R2 Subunit of *Escherichia coli* Ribonucleotide Reductase. 2. Evidence for and Consequences of Blocked Electron Transfer in the W48F Variant. *J. Am. Chem. Soc. 122*, 12207–12219.
61. Stubbe, J., Nocera, D. G., Yee, C. S., and Chang, M. C. Y. (2003) Radical Initiation in the Class I Ribonucleotide Reductase: Long-Range Proton-Coupled Electron Transfer? *Chem. Rev. 103*, 2167–2201.
62. Lee, D., Du Bois, J., Petasis, D., Hendrich, M. P., Krebs, C., Huynh, B. H., and Lippard, S. J. (1999) Formation of Fe(III)Fe(IV) Species from the Reaction between a Diiron(II) Complex and Dioxygen: Relevance to Ribonucleotide Reductase Intermediate X. *J. Am. Chem. Soc. 121*, 9893–9894.
63. Rosenzweig, A. C., Frederick, C. A., Lippard, S. J., and Nordlund, P. (1993) Crystal Structure of a Bacterial Non-Haem Iron Hydroxylase that Catalyses the Biological Oxidation of Methane. *Nature 366*, 537–543.